Supporting information for

Catalytic Conversion of NO and CO into N_2 and CO_2 by Rhodium-Aluminum Oxides in the Gas Phase

Jiao-Jiao Chen,[ac] Xiao-Na Li,*[ac] Li-Hui Mou,[abc] Qing-Yu Liu,[ac] and Sheng-Gui He*[abc]

[a]State Key Laboratory for Structural Chemistry of Unstable and Stable Species, Institute of Chemistry, Chinese Academy of Sciences, Beijing 100190, China.

[b]University of Chinese Academy of Sciences, Beijing 100049, China.

[c]Beijing National Laboratory for Molecular Sciences and CAS Research/Education Center of Excellence in Molecular Sciences, Beijing 100190, China.

*E-mail: lxn@iccas.ac.cn; shengguihe@iccas.ac.cn

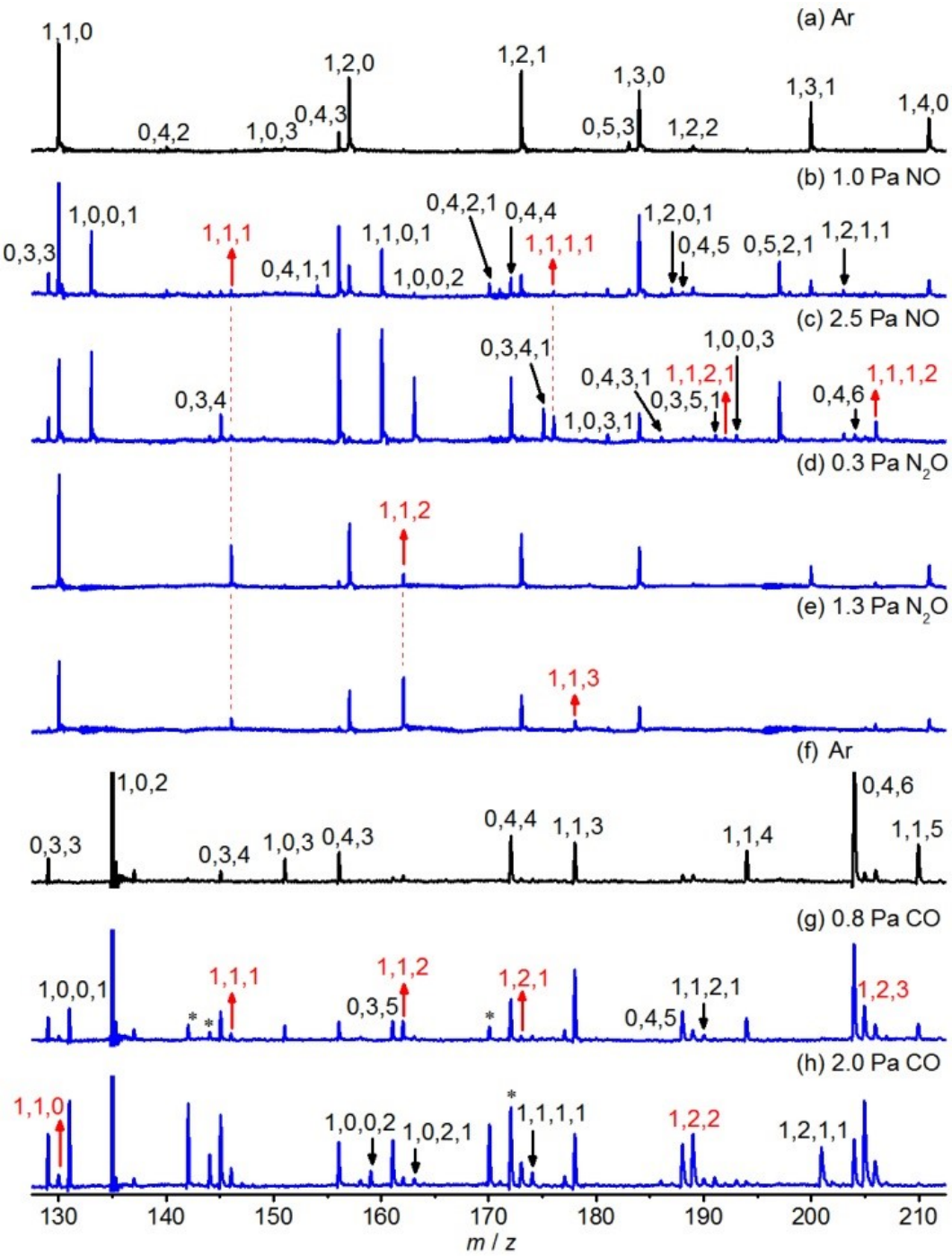

Figure S1. The time-of-flight (TOF) mass spectra for the reactions of neutral $Rh_xAl_yO_z$ species with Ar (a, f), NO (b, c), N_2O (d, e), and CO (g, h). The reactant gas pressures are shown and the reaction time is 60 μs. The $Rh_xAl_yO_z$ and the $Rh_xAl_yO_z$,*n*NO, $Rh_xAl_yO_z$,*n*CO species are denoted as *x*,*y*,*z* and *x*,*y*,*z*,*n*, respectively. The peaks marked with * are the impurities from CO gas.

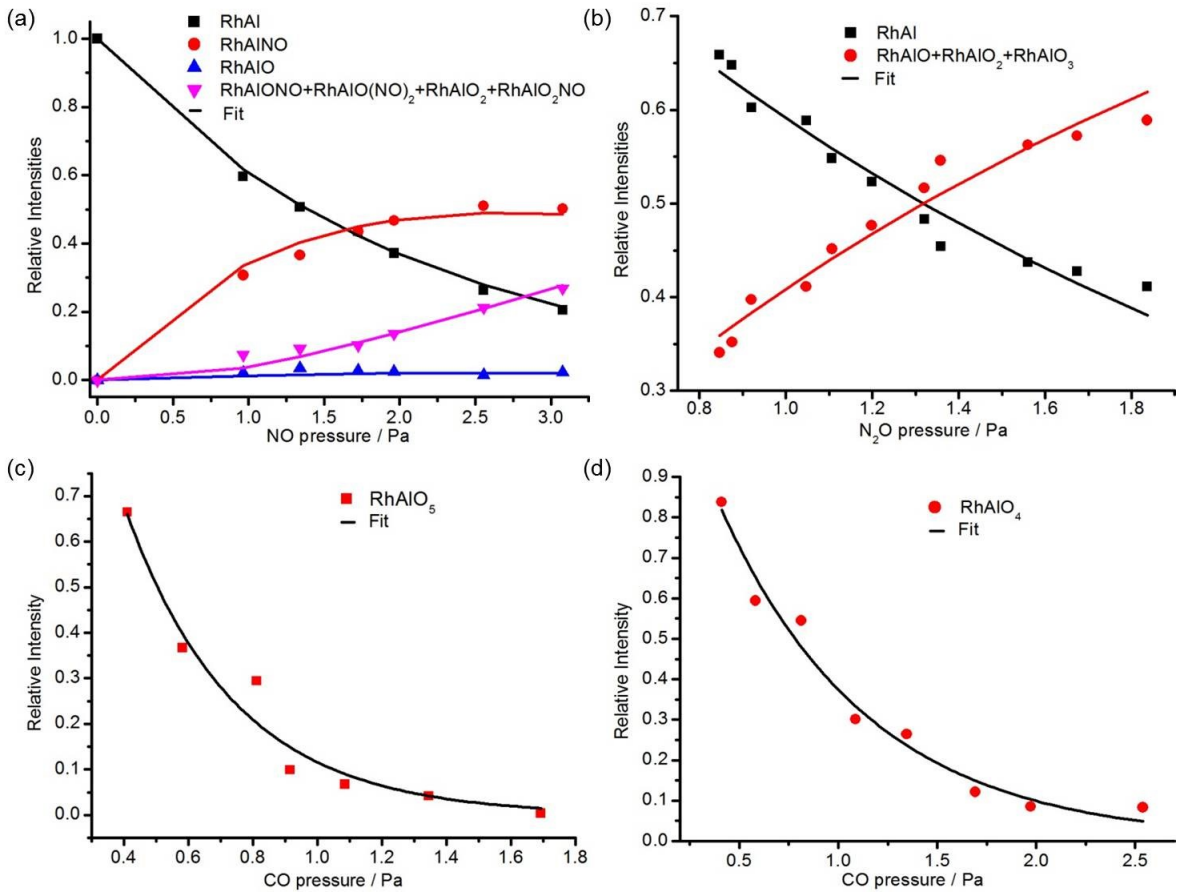

Figure S2. The variations of cluster intensities with respect to the partial pressures of NO and N_2O in the reactions of RhAl with NO (a) and N_2O (b). The depletion of cluster intensities with respect to the partial pressure of CO in the reactions of $RhAlO_5$ (c) and $RhAlO_4$ (d) with CO. The data points were experimentally measured and the solid lines were calculated on the basis of rate constants determined from least-squares fitting.

For the reaction of RhAl with NO (Figure 1B, C and Figure S1b, c), the model RhAl → RhAlNO → RhAlO → RhAlONO + $RhAlO(NO)_2$ + $RhAlO_2$ + $RhAlO_2NO$ was used to fit the cluster intensities obtained from the experiments. The fitted rate constants in unit of 10^{-11} cm^3 $molecule^{-1}$ s^{-1} are k (RhAl + NO → RhAlNO) = 3.4 ± 0.2, k (RhAlNO + NO → RhAlO + N_2O) = 1.8 ± 0.1, k (RhAlO + NO → RhAlONO + $RhAlO(NO)_2$ + $RhAlO_2$ + $RhAlO_2NO$) = 42 ± 14. For the reaction of RhAl with N_2O (Figure 1D, E and Figure S1d, e), the fitted rate constant is (3.3 ± 0.2) × 10^{-11} cm^3 $molecule^{-1}$ s^{-1}. For the reactions of $RhAlO_z$ with CO, the rate constants that were roughly determined by the depletion of $RhAlO_5$ and $RhAlO_4$ are (2.0 ± 0.3) and (0.9 ± 0.1) × 10^{-11} cm^3 $molecule^{-1}$ s^{-1}. The rate constant for $RhAlO_4$ + CO is underestimated because some $RhAlO_4$ may come from the reaction $RhAlO_5$ + CO → $RhAlO_4$ + CO_2. The reaction constants for $RhAlO_z$ (z = 3–1)

also can be roughly estimated and the order of magnitude for the reactions is about 10^{-11} cm^3 $molecule^{-1}$ s^{-1}. The uncertainties (± δ) given above are standard errors in the least-square fitting. The uncertainties of the absolute rate constants are about 40% taking into account the systematic errors of the reaction time and reactant gas pressure. Note that the additional errors for the reactions of neutral RhAl with NO and N_2O can arise if one considers that ionization efficiencies of the reactant and product species are different.

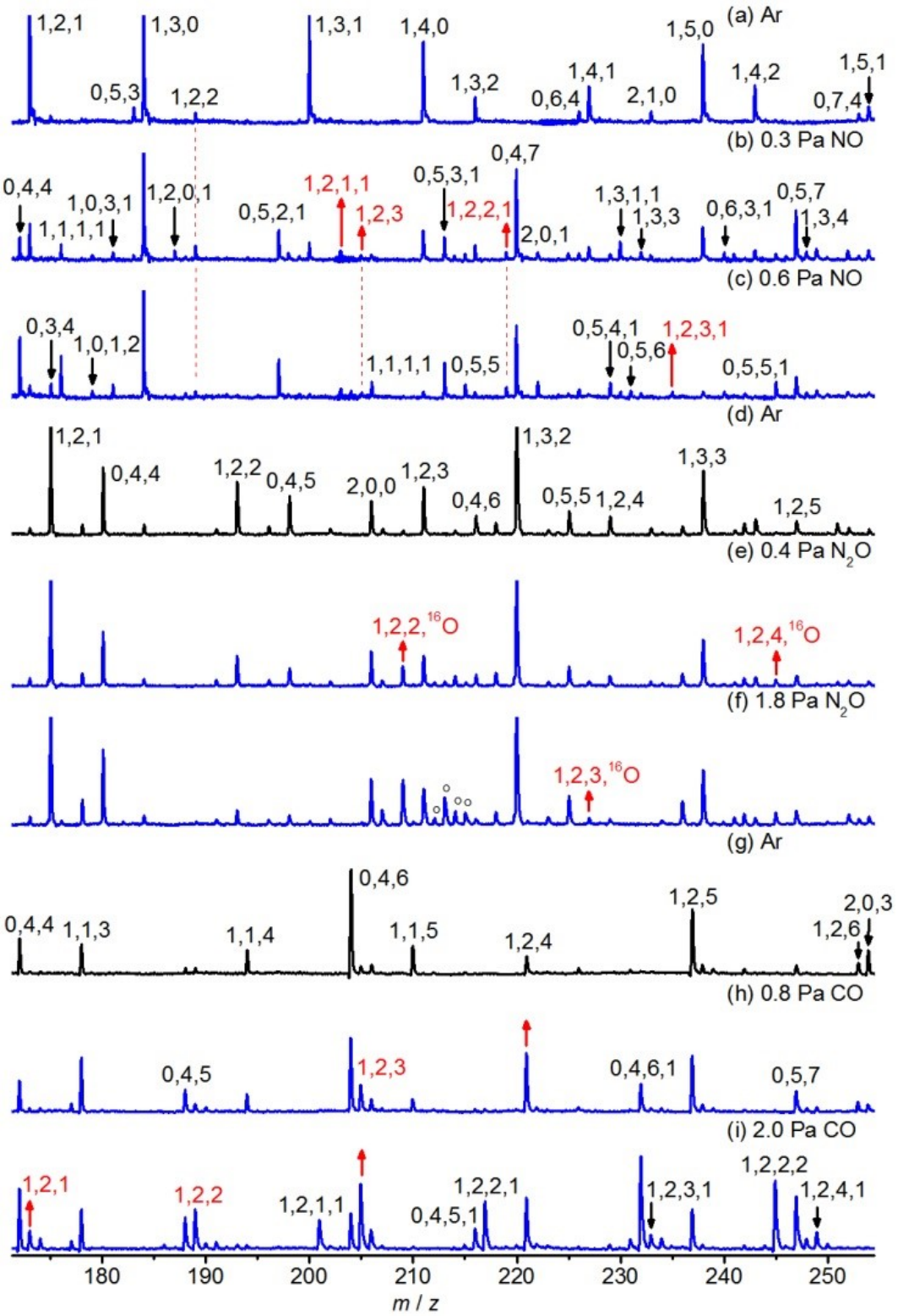

Figure S3. The TOF mass spectra for the reactions of neutral $Rh_xAl_y{}^{16}O_z$ species with Ar (a, g), NO (b, c) and CO (h, i) as well as $Rh_xAl_y{}^{18}O_z$ species with Ar (d) and N_2O (e, f). The reactant gas pressures are shown and the reaction time is 60 μs. The $Rh_xAl_y{}^{16}O_z$, $Rh_xAl_y{}^{18}O_z$ and the $Rh_xAl_y{}^{16}O_z$,nNO, $Rh_xAl_y{}^{16}O_z$,nCO species are denoted as x,y,z and x,y,z,n, respectively. The $Rh_xAl_y{}^{18}O_z{}^{16}O$ species is labeled as x,y,z,^{16}O. The peaks marked with o are the impurities from the reactions of $Al_y{}^{18}O_z$ with N_2O.

Neutral species cannot be mass selected and the different reactivity of $Rh_xAl_yO_z$ towards reactants makes it difficult to study all the $Rh_xAl_yO_z$ species under the same experimental conditions. In this case, different experimental conditions were performed to explore the reactivity of $RhAl_2O_z$ (Figure S3). On the interactions of $RhAl_2O_z$ with NO (Figure S3b), new product peaks $RhAl_2ONO$ (1,2,1,1), $RhAl_2O_2NO$ (1,2,2,1), and $RhAl_2O_3$ (1,2,3) appeared, at the same time, the signal intensity of $RhAl_2O$ (1,2,1) decreased obviously and the intensity of peak $RhAl_2O_2$ (1,2,2) increased. With the increase of NO partial pressure (Figure S3c), new product $RhAl_2O_3NO$ (1,2,3,1) can also be observed. Based on these experimental results, we propose that $RhAl_2O_{1,2}$ can pick up a NO molecule to generate $RhAl_2O_{1,2}NO$ (reaction S1a), which then captures and reacts with a second NO molecule to produce $RhAl_2O_{2,3}$ and N_2O (reaction S1b). Figure S2d-f show that upon the reactions of $RhAl_2{}^{18}O_z$ with N_2O, new signals $RhAl_2{}^{18}O_z{}^{16}O$ (z = 2–4) appeared, while the intensities of $RhAl_2{}^{18}O_z$ (z = 2–4) decreased simultaneously, indicating that N_2O can be reduced by $RhAl_2O_{2–4}$ to produce N_2 (reaction S2). On the interactions of $RhAl_2O_z$ with CO (Figure S3h, i), signal intensities of $RhAl_2O_6$ and $RhAl_2O_5$ decreased significantly, while those of $RhAl_2O_4$ and $RhAl_2O_3$ increased simultaneously. Moreover, new signals $RhAl_2O_2$ and $RhAl_2O$ appeared with the increase of CO pressure. These experiments evidenced that $RhAl_2O_6$ can oxidize five CO molecules consecutively to regenerate $RhAl_2O$ (reaction S3). Thus, the conversion of NO and CO into N_2 and CO_2 can be also catalyzed by the neutral $RhAl_2O_{1–4}$ species. Similarly, the rate constants for reactions S1-S3 have been roughly estimated and the order of magnitude is about 10^{-11} cm^3 $molecule^{-1}$ s^{-1}.

$$RhAl_2O_z + NO \rightarrow RhAl_2O_zNO \qquad (z = 1, 2) \qquad \text{(S1a)}$$

$$RhAl_2O_zNO + NO \rightarrow RhAl_2O_{z+1} + N_2O \qquad (z = 1, 2) \qquad \text{(S1b)}$$

$$RhAl_2O_z + N_2O \rightarrow RhAl_2O_{z+1} + N_2 \qquad (z = 2–4) \qquad \text{(S2)}$$

$$RhAl_2O_z + CO \rightarrow RhAl_2O_{z-1} + CO_2 \qquad (z = 6–2) \qquad \text{(S3)}$$

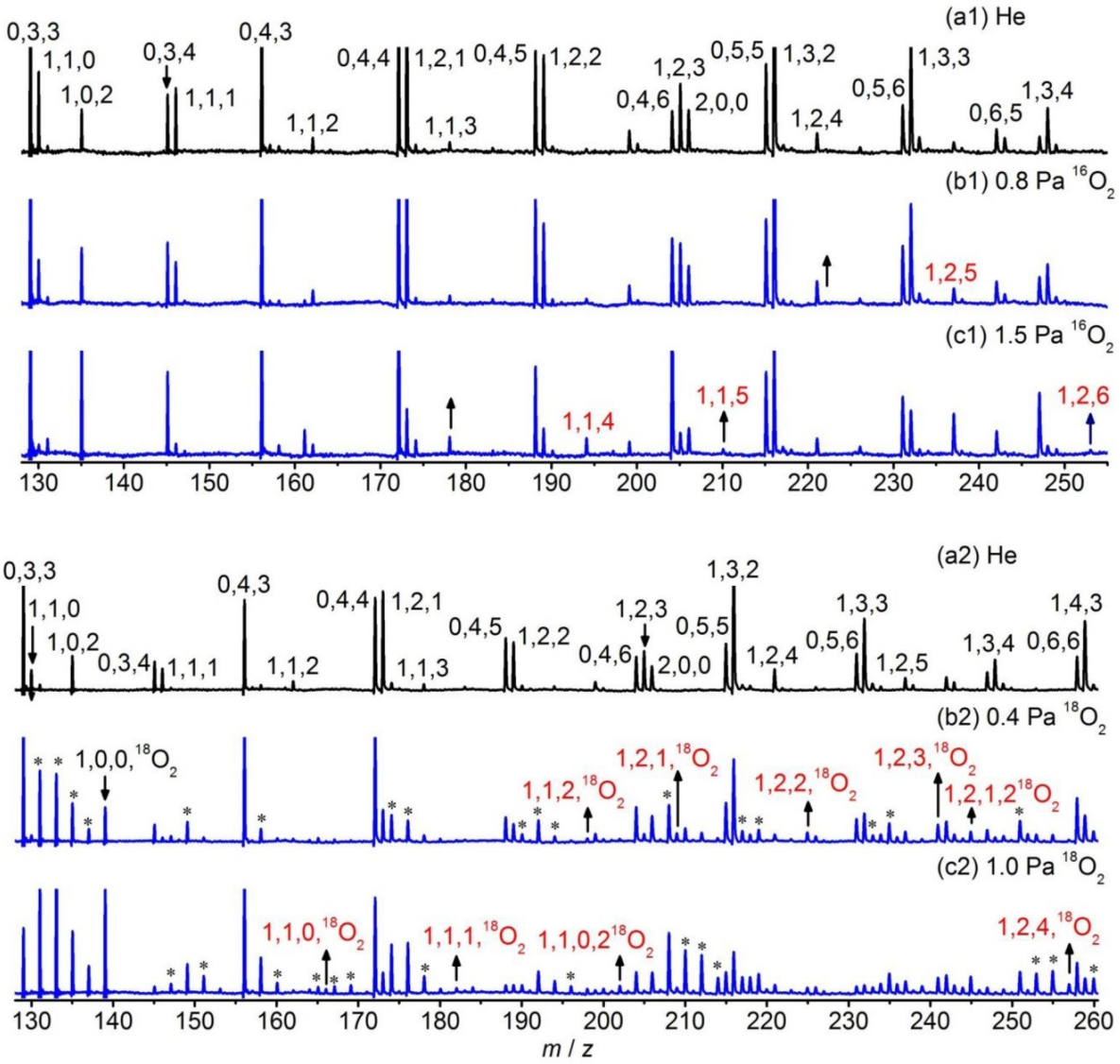

Figure S4. The TOF mass spectra for the reactions of neutral $Rh_xAl_y{}^{16}O_z$ species (a1, a2) with $^{16}O_2$ (b1, c1) and $^{18}O_2$ (b2, c2). The reactant gas pressures are shown and the reaction time is about 60 μs. The $Rh_xAl_y{}^{16}O_z$ and $Rh_xAl_y{}^{16}O_z,n^{18}O_2$ species are denoted as x,y,z and $x,y,z,n^{18}O_2$, respectively. The peaks marked with * are the impurities from the reactions of $Al_y{}^{16}O_z$ with $^{18}O_2$.

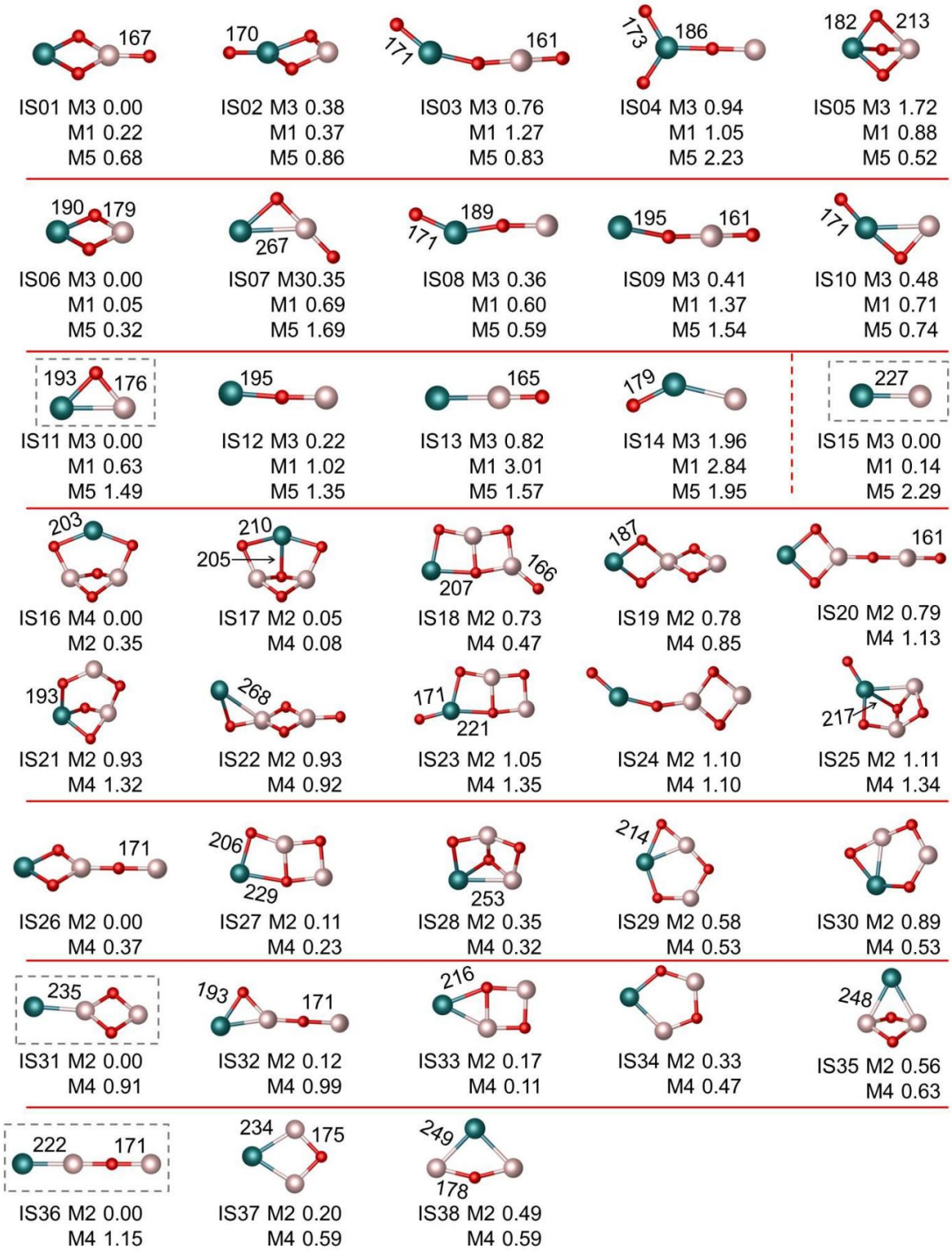

Figure S5. The Density functional theory (DFT) optimized isomers of neutral $RhAlO_{3-0}$ and $RhAl_2O_{4-1}$ species. The relative energies (in eV, zero-point vibrational corrected) are listed below each isomer and bond lengths are given in pm.

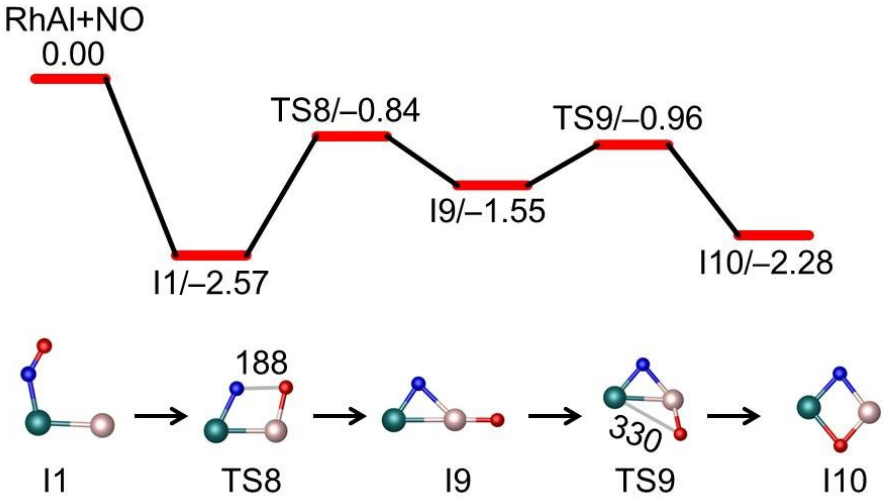

Figure S6. The DFT-calculated potential energy profile for reaction RhAl + NO. Bond lengths and relative energies are in units of pm and eV, respectively.

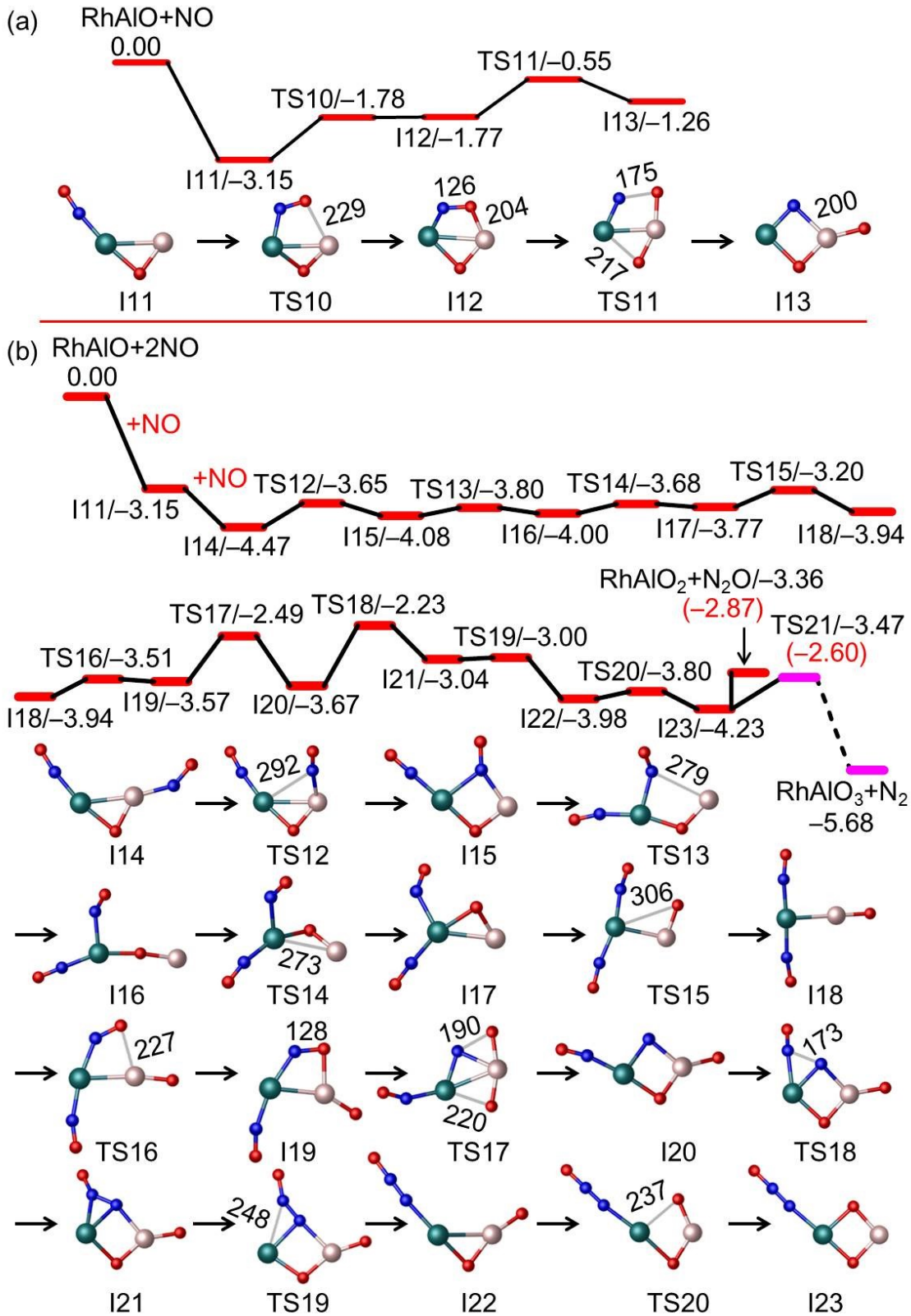

Figure S7. The DFT-calculated potential energy profiles for reactions RhAlO + NO (a) and RhAlO + 2NO (b). Bond lengths and relative energies are in units of pm and eV, respectively. The values in parentheses are calculated Gibbs free energies at T = 298 K.

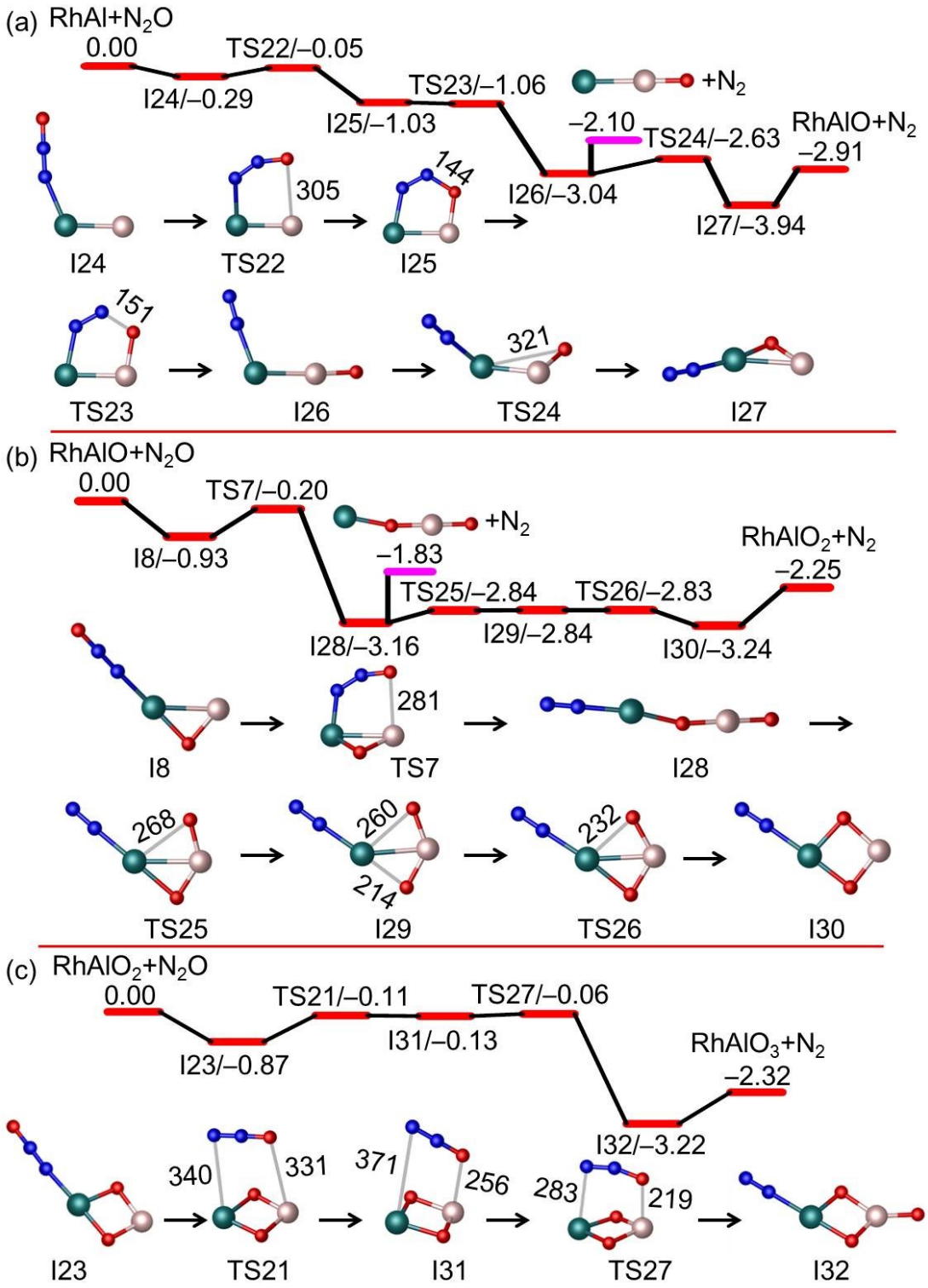

Figure S8. The DFT-calculated potential energy profiles for the reactions of RhAl (a), RhAlO (b), and $RhAlO_2$ (c) with N_2O. Bond lengths and relative energies are in units of pm and eV, respectively.

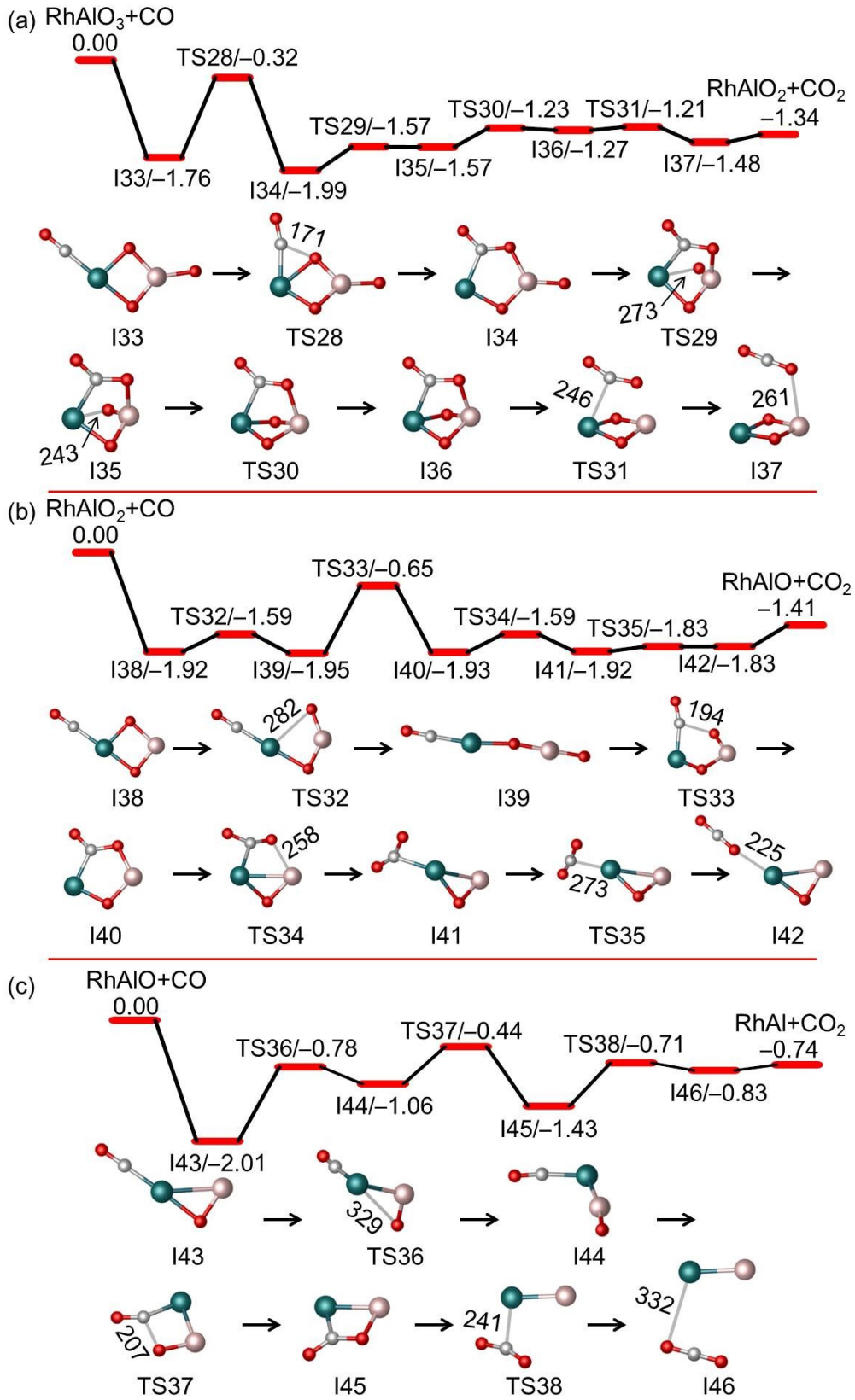

Figure S9. The DFT-calculated potential energy profiles for the reactions of $RhAlO_3$ (a), $RhAlO_2$ (b) and RhAlO (c) with CO. Bond lengths and relative energies are in units of pm and eV, respectively.

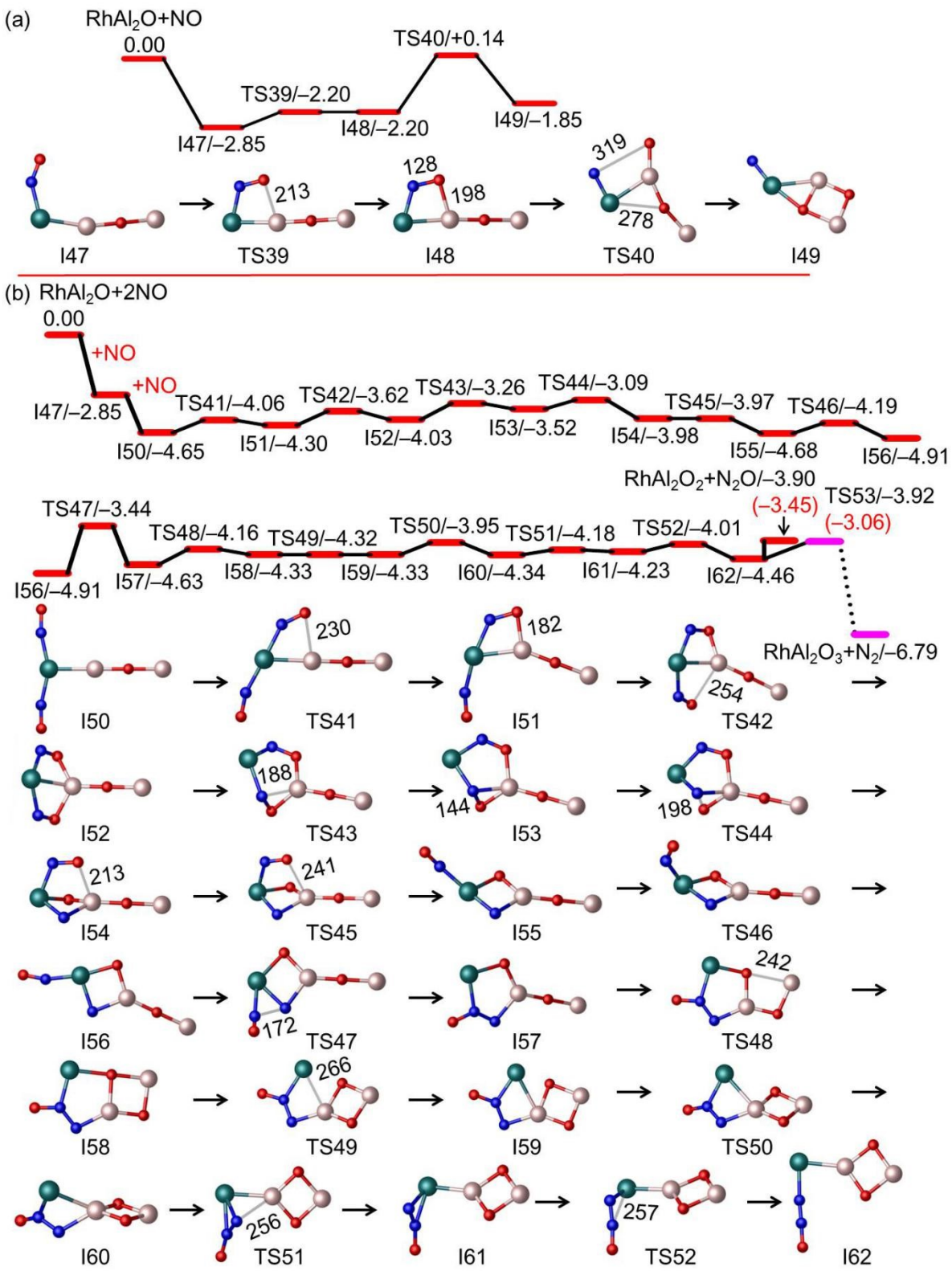

Figure S10. The DFT-calculated potential energy profiles for reactions $RhAl_2O$ + NO (a) and $RhAl_2O$ + 2NO (b). Bond lengths and relative energies are in units of pm and eV, respectively. The values in parentheses are calculated Gibbs free energies at T = 298 K.

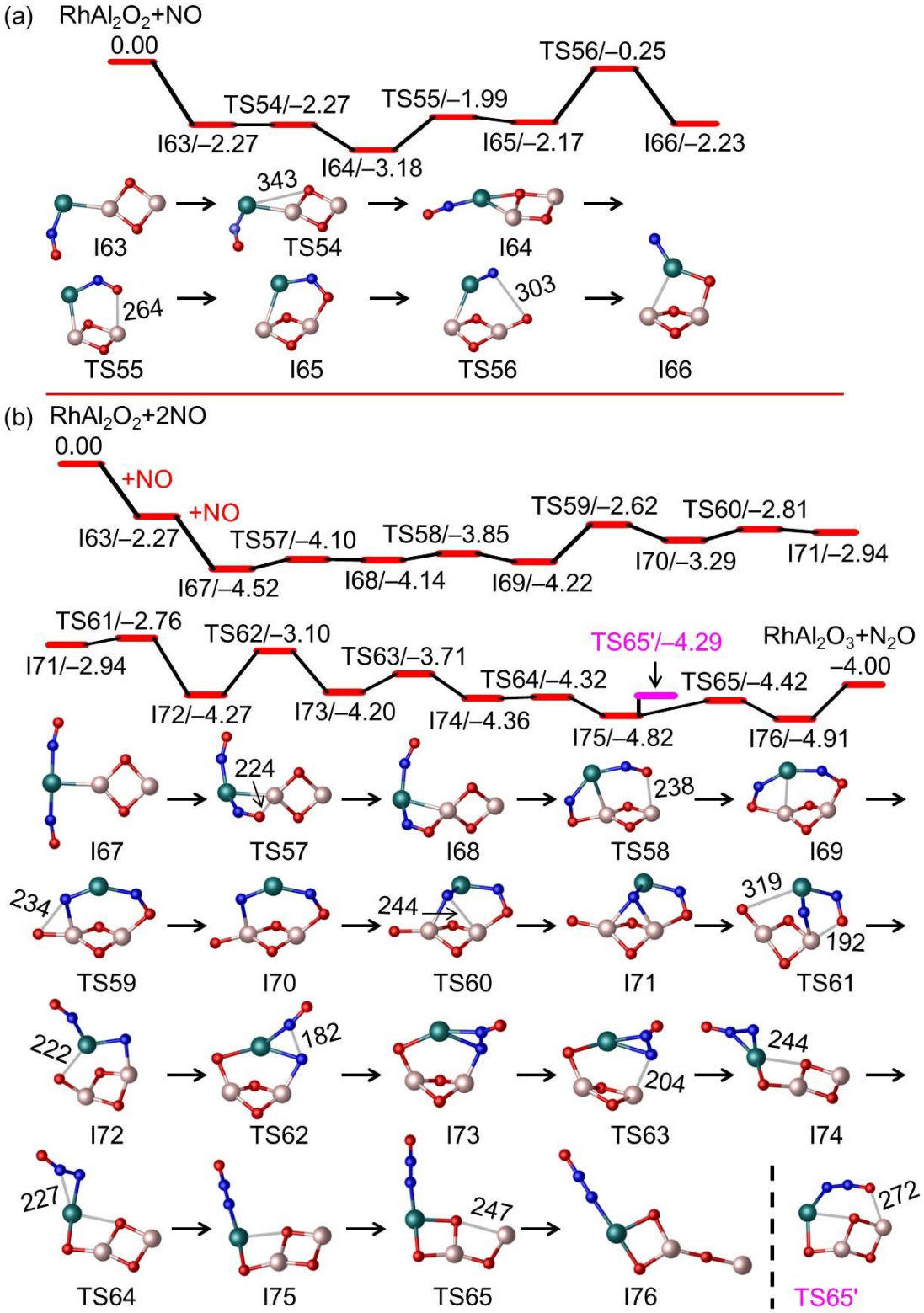

Figure S11. The DFT-calculated potential energy profiles for reactions $RhAl_2O_2$ + NO (a) and $RhAl_2O_2$ + 2NO (b). Bond lengths and relative energies are in units of pm and eV, respectively.

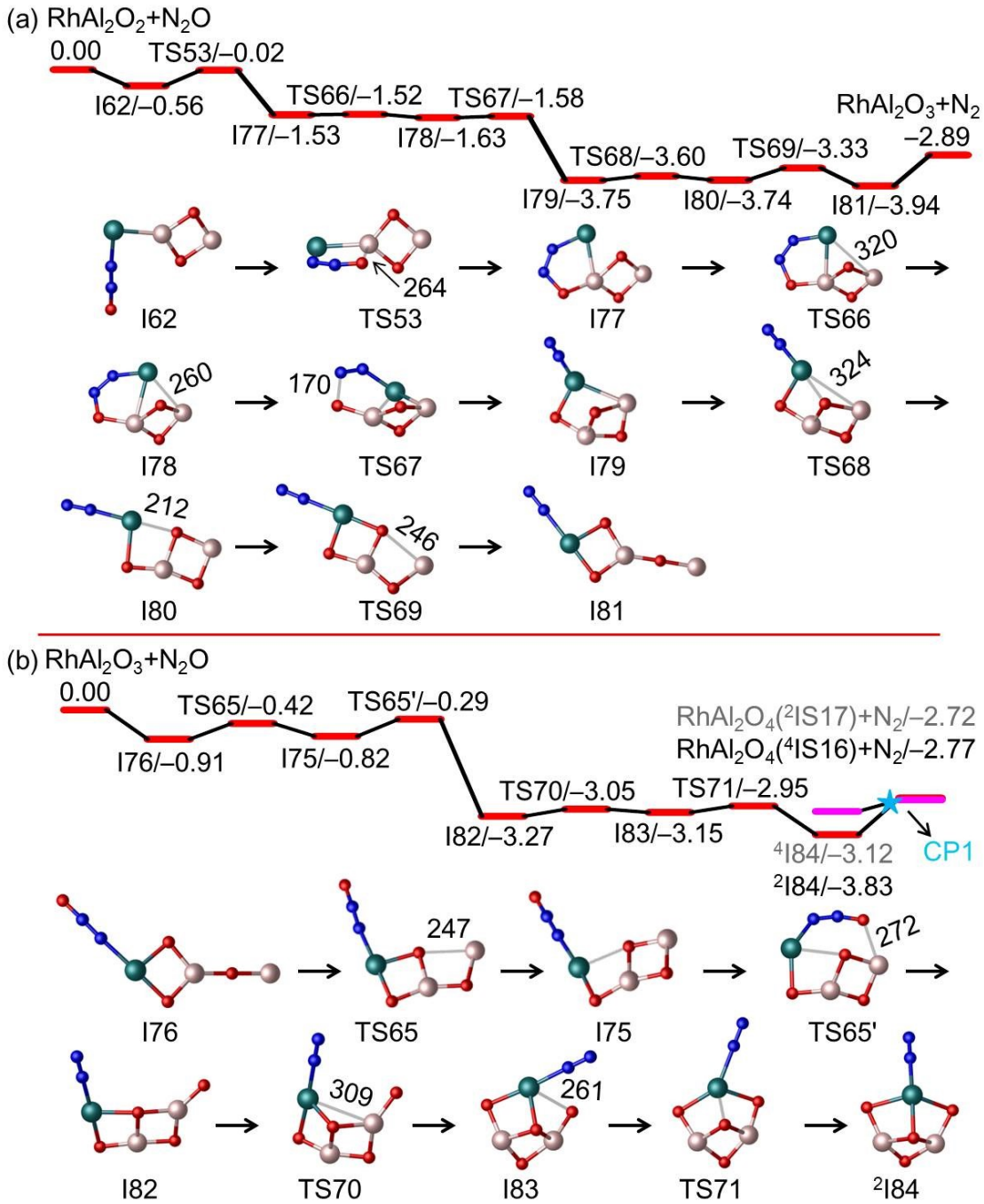

Figure S12. The DFT-calculated potential energy profiles for the reactions of $RhAl_2O_2$ (a) and $RhAl_2O_3$ (b) with N_2O. The superscript denotes spin multiplicity. The crossing point (CP1) appearing in the spin conversion is shown in Figure S15a. Bond lengths and relative energies are in units of pm and eV, respectively.

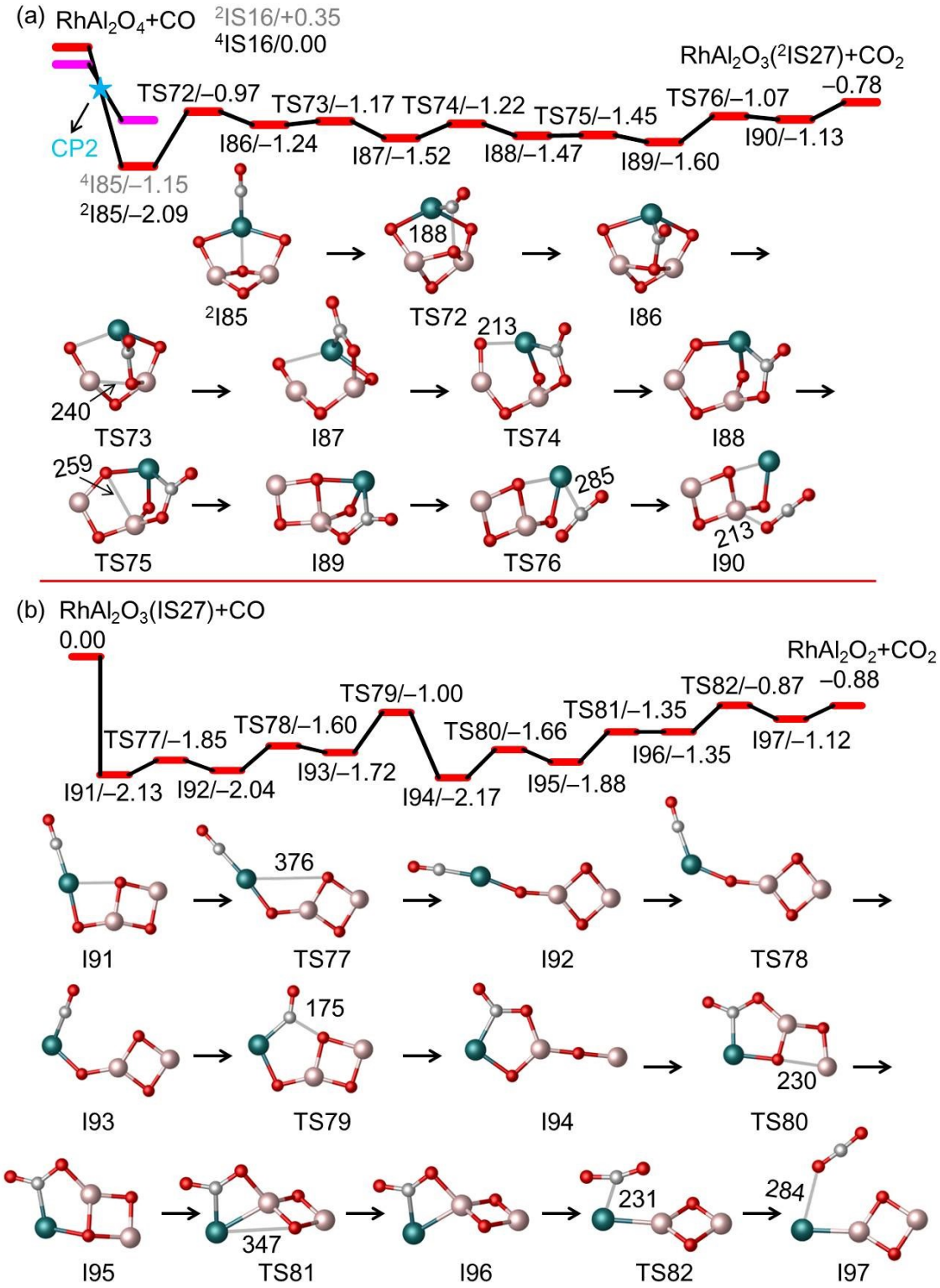

Figure S13. The DFT-calculated potential energy profiles for CO oxidation by $RhAl_2O_4$ (a) and the resulting product $RhAl_2O_3$ (IS27, Figure S5) (b). The superscript denotes spin multiplicity. The crossing point (CP2) appearing in the spin conversion is shown in Figure S15b. Bond lengths and relative energies are in units of pm and eV, respectively.

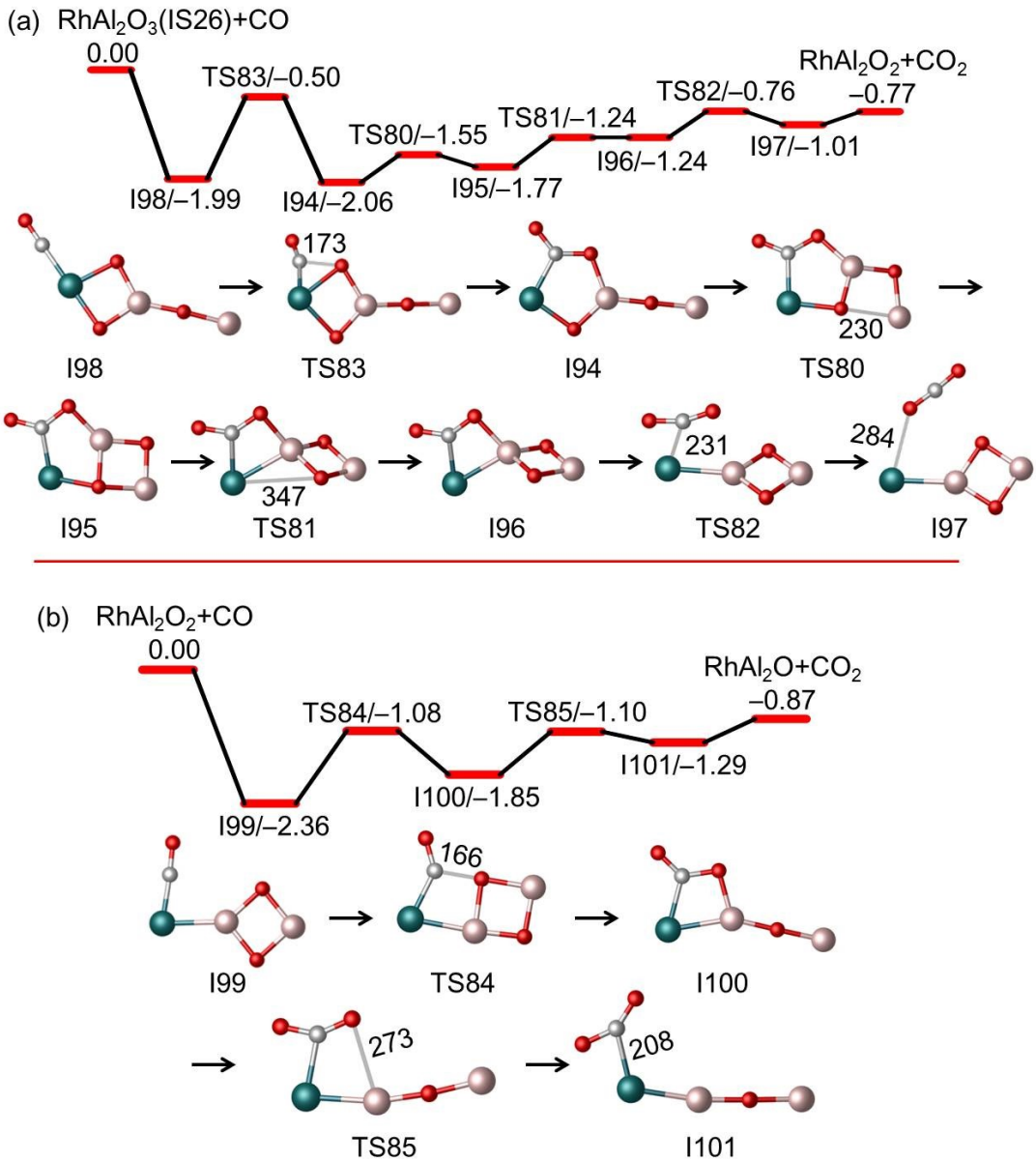

Figure S14. The DFT-calculated potential energy profiles for CO oxidation by the most stable $RhAl_2O_3$ isomer (IS26, Figure S5) (a) and $RhAl_2O_2$ (b). Bond lengths and relative energies are in units of pm and eV, respectively.

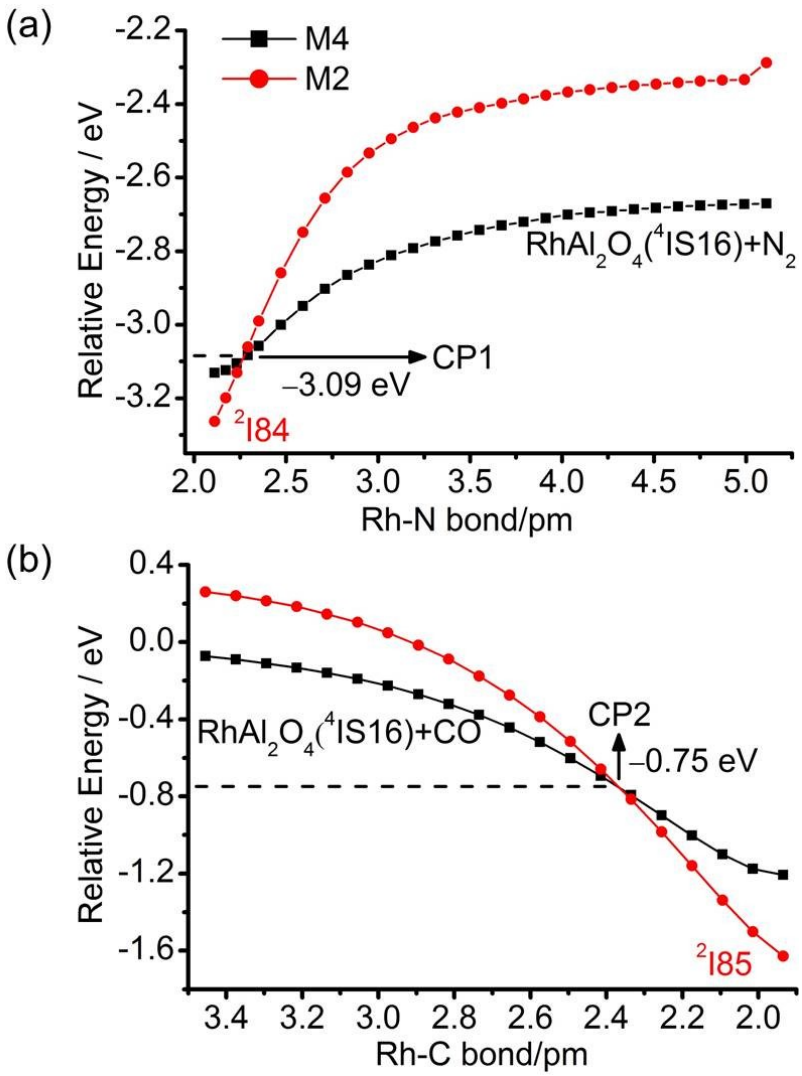

Figure S15. The DFT-calculated potential-energy curves (PECs) for spin conversions in Figures S12b and S13a. The fill square lines in (a, b) are the relaxed PECs obtained by scan calculations staring from ^{4}I84 to products and ^{4}I85 to separate reactants, respectively. The optimized geometries from filled square lines in (a, b) were used for single-point energy calculations of doublet (filled circle line), respectively. The electronic energies of the crossing points (CP1 and CP2) relative to the corresponding separated reactants are given.

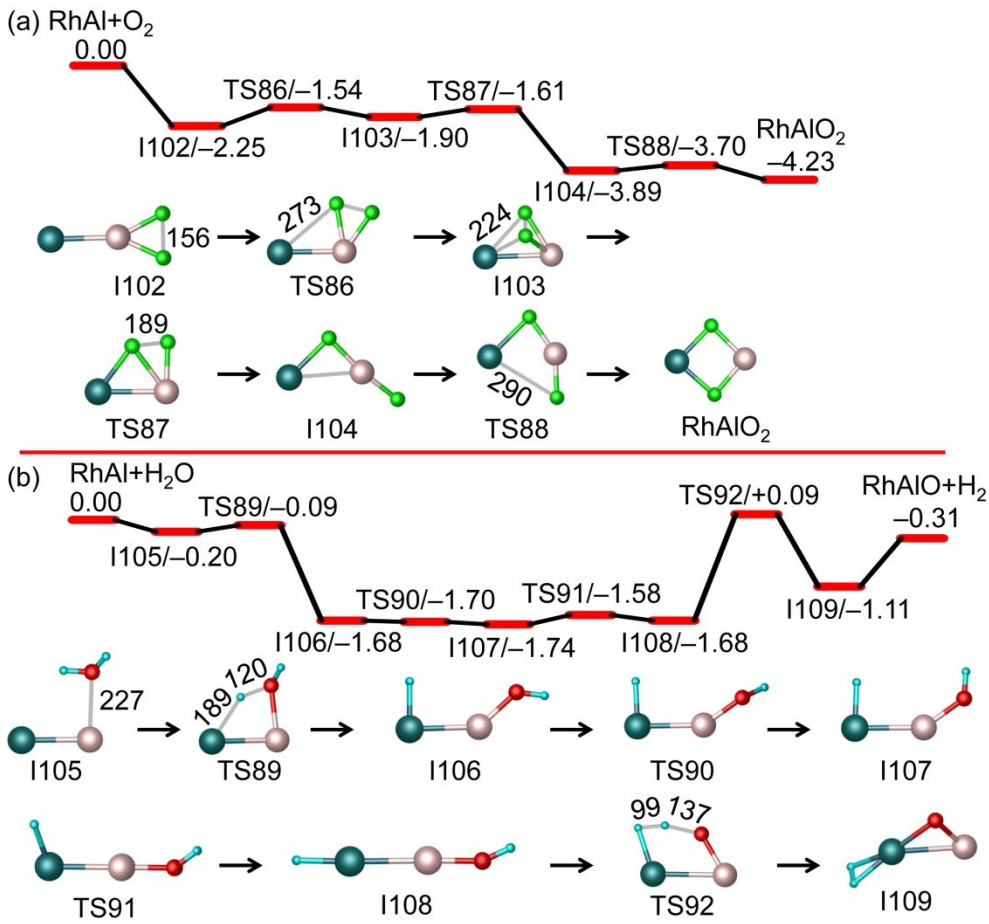

Figure S16. The DFT-calculated potential energy profiles for reactions RhAl + O_2 (a) and RhAl + H_2O (b). Bond lengths and relative energies are in units of pm and eV, respectively.

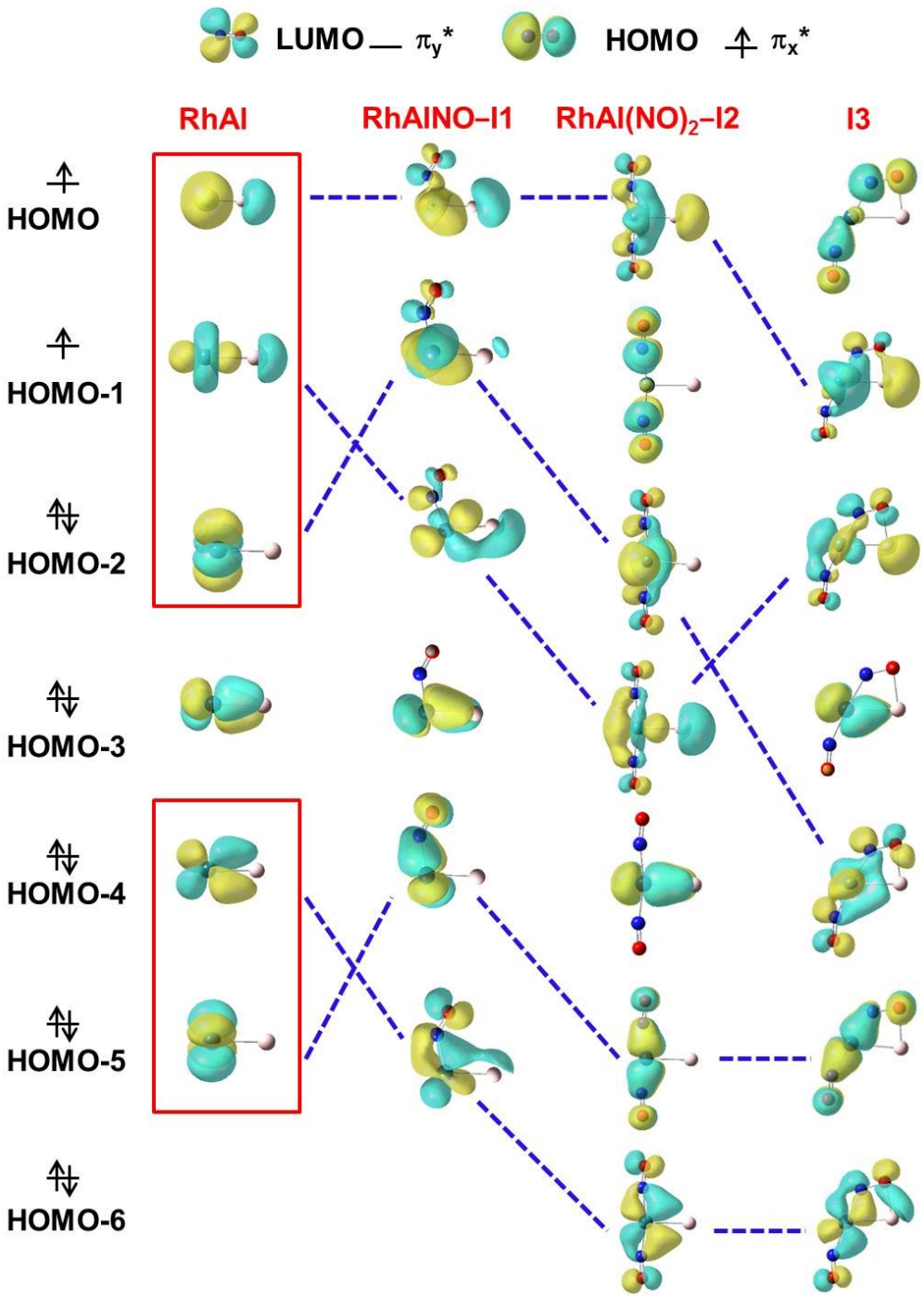

Figure S17. Frontier molecular orbitals for RhAl and intermediates I1–I3 in Figure 2B of the main text. The highest occupied molecular orbital and lowest unoccupied molecular orbital are denoted as HOMO and LUMO, respectively.

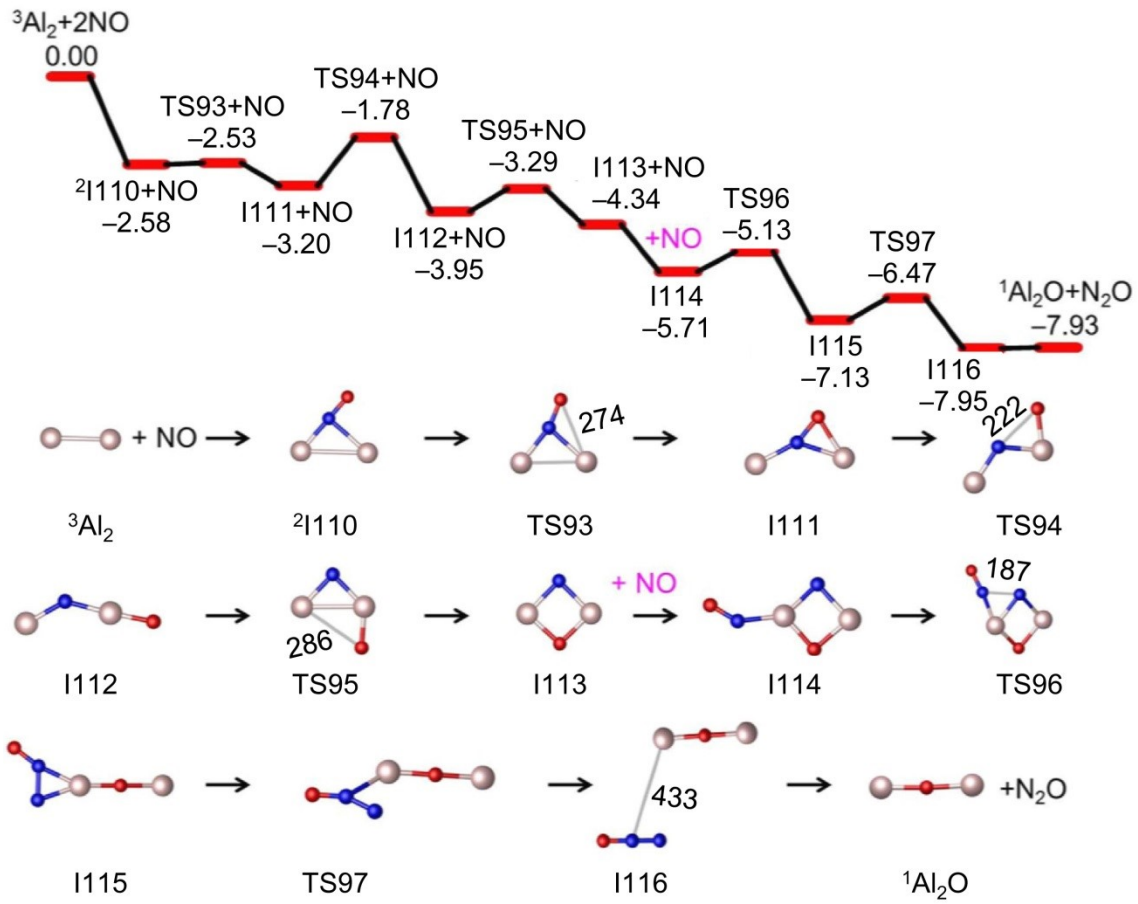

Figure S18. The DFT-calculated potential energy profile for reaction Al_2 + 2NO. The superscript denotes spin multiplicity. Bond lengths and relative energies are in units of pm and eV, respectively.